

Coexistence of high electron-mobility, unpaired spins, and superconductivity at high carrier density SrTiO₃-based interfaces

Thor Hvid-Olsen,¹ Christina H. Christoffersen,¹ Damon J. Carrad,¹ Nicolas Gauquelin,² Dāgs Olšteins,¹ Johan Verbeeck,² Nicolas Bergeal,³ Thomas S. Jespersen,¹ and Felix Trier^{†1}

¹*Department of Energy Conversion and Storage,*

Technical University of Denmark, Fysikvej 310 DK-2800 Kgs. Lyngby, Denmark.

²*Electron Microscopy for Materials Science (EMAT), University of Antwerp, Antwerp, Belgium.*

³*Laboratoire de Physique et d'Etude des Matériaux, ESPCI Paris,*

Université PSL, CNRS, Sorbonne Université, Paris, France.

(Dated: November 7, 2024)

The $t2g$ band-structure of SrTiO₃-based two-dimensional electron gasses (2DEGs), have been found to play a role in features such as the superconducting dome, high-mobility transport, and the magnitude of spin-orbit coupling. This adds to the already very diverse range of phenomena, including magnetism and extreme magnetoresistance, exhibited by this particular material platform. Tuning and/or combining these intriguing attributes could yield significant progress within quantum and spintronics technologies. Doing so demands precise control of the parameters, which requires a better understanding of the factors that affect them. Here we present effects of the $t2g$ band-order inversion, stemming from the growth of spinel-structured γ -Al₂O₃ onto perovskite SrTiO₃. Electronic transport measurements show that with LaAlO₃/SrTiO₃ as the reference, the carrier density and electron mobility are enhanced, and the sample displays a reshaping of the superconducting dome. Additionally, unpaired spins are evidenced by increasing Anomalous Hall Effect with decreasing temperature, entering the same temperature range as the superconducting transition, and a Kondo-like upturn in the sheet resistance. Finally, it is argued that the high-mobility dxz/yz -band is more likely than the dxy -band to host the supercurrent.

I. INTRODUCTION

Oxide-based two-dimensional electron gases (2DEGs) display a wide range of intriguing phenomena, including superconductivity[5–7], Josephson-Junction-like dynamics,[8, 9] ferromagnetism,[10], tunable spin-orbit coupling[11], high-mobility transport,[12, 13], coexistence of ferromagnetism and superconductivity,[14–16], and spin-charge interconversion.[17–19] In addition, LaAlO₃/SrTiO₃ has been proposed as a platform for topological superconductivity and spin polarizers.[20] One origin contributing to this functional diversity stems from the rich d -orbital nature of transition metal oxides. In fact, the band structure of LaAlO₃/SrTiO₃ alone has explained phenomena as s_{\pm} -wave superconductivity[21, 22], gate electrode location dependent splitting of the superconducting (SC) critical temperature (T_C) as a function of 2D carrier concentration [23], unconventional tuning of critical current (I_C) by magnetic field,[24], and the superconducting dome of T_C as a function of carrier density.[21–23]

Usually, SrTiO₃-based interface 2DEGs are realized by growing top layers of e.g. LaAlO₃ onto TiO₂-terminated SrTiO₃-substrates. With its octahedral ordering, the electronic $3d$ bands of the Ti in SrTiO₃ split into three $t2g$ states and two higher eg states. The $t2g$ states correspond to the dxy, xz, yz -orbitals and their degeneracy is lifted by inversion symmetry breaking due to the thin film on top. For LaAlO₃/SrTiO₃ this elevates the energy of the dxz/yz -band relative to the dxy -band.[25, 26] Since the Fermi Energy of these

metallic SrTiO₃-based 2DEGs is located at the energies of the dxy, xz, yz -bands, the lowering of the dxy -band renders this particular band the most dominant in terms of electronic transport. However, recent studies have revealed how band-reordering can be achieved by engineering epitaxial growth, which can explain the higher charge carrier mobility (μ) in γ -Al₂O₃/SrTiO₃ compared to LaAlO₃/SrTiO₃. [4, 27–29]

At temperatures below 5 K, the main scattering contributions limiting μ in SrTiO₃ 2DEGs come from intentional ionized impurities incorporated into SrTiO₃, defects, and/or surface roughness.[13, 30] Oxygen vacancies act as both dopants for the 2DEG and scattering sites. This has motivated several studies of the relation of the spatial distribution of oxygen vacancies and the 2DEG.[31–33] Here, the band-ordering is crucial as the spatial separation between the oxygen vacancies and charge carriers, in the dxz/yz bands, on average is larger than for the dxy -band. The explanation is that the oxygen vacancies are primarily located at or near the interface, which largely overlaps with the spatial extent of the dxy -band. In contrast, the dxz/yz -band extends deeper into SrTiO₃ and therefore further away from the interfacial oxygen vacancies. One possible reason for the band inversion is the spinel structure of γ -Al₂O₃ causing the octahedral ordering of Ti to change to a pyramidal ordering at the interface, breaking the $t2g$ symmetry, and flipping the band-ordering of the dxy, xz, yz -bands. In contrast, the perovskite LaAlO₃ sustains the octahedral ordering of Ti.[27]

This study further explores outcomes of band-ordering in SrTiO₃-based 2DEGs, by comparing the systems of

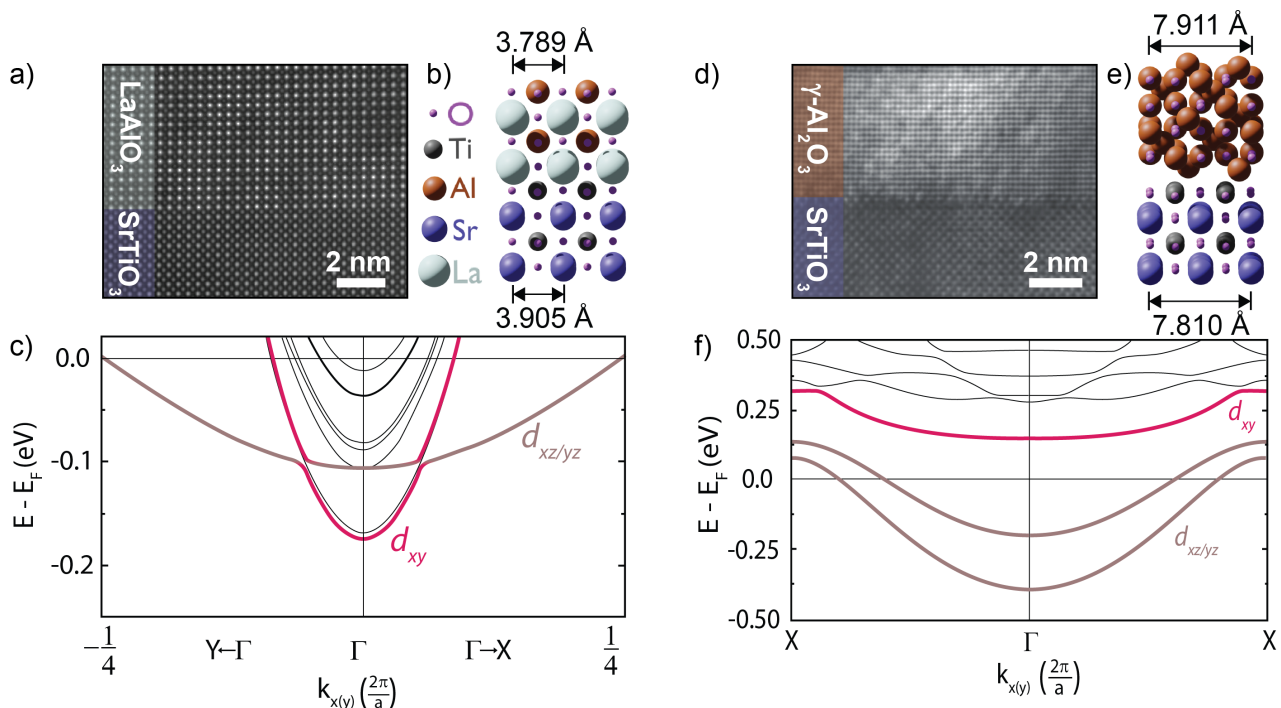


FIG. 1. Comparison of the band and crystal structure of $\text{LaAlO}_3/\text{SrTiO}_3$ and $\gamma\text{-Al}_2\text{O}_3/\text{SrTiO}_3$. False-color HRSTEM of the $\text{LaAlO}_3/\text{SrTiO}_3$ a) and $\gamma\text{-Al}_2\text{O}_3/\text{SrTiO}_3$ d) interfaces displaying high ordering and local crystallinity. Crystal structure of the $\text{LaAlO}_3/\text{SrTiO}_3$ b) and $\gamma\text{-Al}_2\text{O}_3/\text{SrTiO}_3$ e) interfaces, with indications of the difference in lattice constants. Lattice constants found in refs [1, 2]. DFT-calculated band structures of $\text{LaAlO}_3/\text{SrTiO}_3$ c) and $\gamma\text{-Al}_2\text{O}_3/\text{SrTiO}_3$ f) displaying the band-inversion that arise in $\gamma\text{-Al}_2\text{O}_3/\text{SrTiO}_3$ in contrast to $\text{LaAlO}_3/\text{SrTiO}_3$. c) is adapted from ref. [3] and f) from ref.[4].

$\text{LaAlO}_3/\text{SrTiO}_3$ and $\gamma\text{-Al}_2\text{O}_3/\text{SrTiO}_3$. We examine theoretically the qualitative differences between the band structures of the crystals and present detailed magnetotransport measurements of sheet and Hall resistance, and superconductivity of a high-mobility $\gamma\text{-Al}_2\text{O}_3/\text{SrTiO}_3$ 2DEG. Furthermore, the relation between charge carrier density, n_s , mobility, and superconducting critical temperature, T_C , of $\gamma\text{-Al}_2\text{O}_3/\text{SrTiO}_3$ is discussed and compared to previous studies. Based on the two $\gamma\text{-Al}_2\text{O}_3/\text{SrTiO}_3$ samples measured in this study, we arrive at indications of a novel reshaping of the superconducting dome with the changed band-ordering. Taking Anomalous Hall Effect (AHE) and Kondo-like features in the electronic transport data into account indicates the coexistence of unpaired spins and superconductivity in the same temperature range. Finally, we discuss the origin of the two-dimensional superconducting phase, whether this arises from the d_{xy} -band or $d_{xz/yz}$ -band, and how this ties into the reshaped superconducting dome.

II. EXPERIMENTAL

Six samples were investigated in this study. Sample 1, 2, 3 and 6 are $\gamma\text{-Al}_2\text{O}_3$ (≈ 5 nm)/ SrTiO_3 (0.5 mm) grown

by Pulsed Laser Deposition (PLD) for 4 min. Sample 1 and 2 was grown with a laser fluence of 9 J/cm^2 and an oxygen partial pressure at 2×10^{-6} mbar, sample 3 was grown with a laser fluence of 6 J/cm^2 at an oxygen partial pressure at 2×10^{-6} mbar. Sample 6 was grown with a laser fluence of 9 J/cm^2 at an oxygen partial pressure at 1×10^{-6} mbar, but with a cooldown pressure after deposition at 1×10^{-7} mbar. Sample 4 is a $\gamma\text{-Al}_2\text{O}_3$ (≈ 34.7 nm)/ SrTiO_3 (0.5 mm) grown with a laser fluence of 9 J/cm^2 at an oxygen partial pressure at 1×10^{-6} mbar for 30 min, and sample 5 is a $\text{LaAlO}_3/\text{SrTiO}_3$ sample grown by Z. Liao at the University of Twente (Twente, The Netherlands) further described in ref. [34]. In the fabrication of samples 1-4 and 6, commercial SrTiO_3 (100) substrates[35] were cleaned using ultrasonication in acetone and isopropanol (IPA), and subsequently annealed in 1 bar O_2 atmosphere with a 60 min dwell time at 1000°C and an up/down ramp rate on 100°C/h . Prior to $\gamma\text{-Al}_2\text{O}_3$ deposition, the substrates were ultrasonicated in acetone:IPA 50:50 for 480 s. The depositions were carried out at 650°C , using a single-crystalline $\alpha\text{-Al}_2\text{O}_3$ target. The PLD used a 248 nm KrF excimer laser and a repetition rate of 1 Hz. Before heating, the chamber was first flushed with oxygen to a pressure of 7×10^{-2} mbar. Then evacuated to a base pressure of $\approx 10^{-7}$ mbar. The pressure was manually maintained during heating, deposition, and initial cooldown, through a valve between the PLD chamber and the turbo

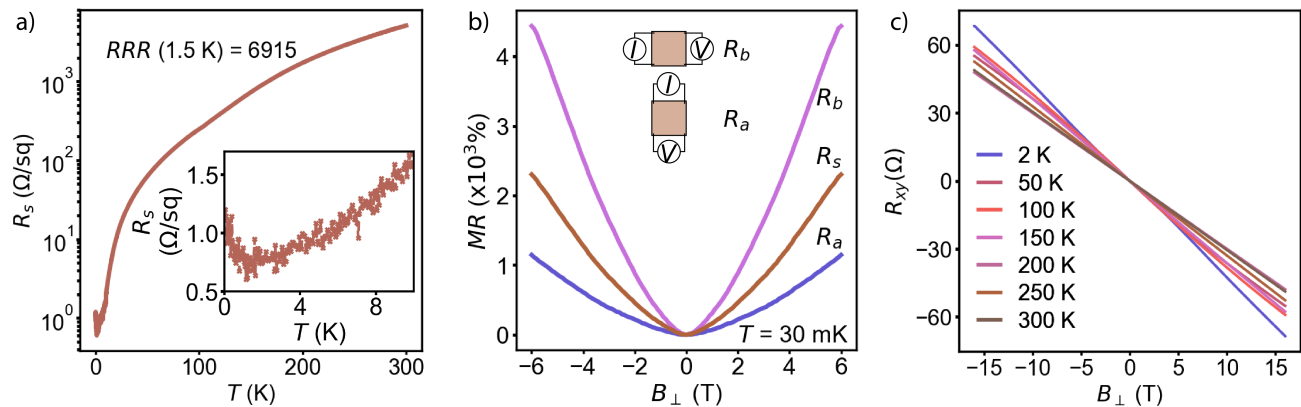


FIG. 2. Temperature and out-of-plane magnetic field dependencies on the resistance. Sheet resistance as a function of temperature in a), magnetoresistance (Hall resistance) as a function of out-of-plane magnetic field in b) (c) at 30 mK (varying temperatures). In b) the insets indicate the measurement configurations R_a and R_b

pump. When the cooldown had reached 300 °C, the system was left to cool to room temperature over 4-5 hours during which time the pressure was decreasing to 5×10^{-7} mbar. Sample 3 and 5 were analyzed using High Resolution Scanning Transmission Electron Microscopy (HRSTEM). The γ -Al₂O₃ growth rates were estimated by X-ray diffraction (XRD) and reflectivity (XRR) measured on sample 4.

Samples 1 and 2 were electrically connected by Al ultrasonic wire-bonding in van der Pauw (vdP) configuration. The electronic measurements above 2 K were performed using a Cryogen-Free Measurement System equipped with a 16 T magnet, and below 2 K, the electronic measurements were performed in a dilution refrigerator with a 6-1-1 T vector magnet. HRSTEM was performed on a Thermofisher Scientific Titan Microscope operated at 300kV. Due to the lower scattering of γ -Al₂O₃ compared to LaAlO₃, images were taken in Medium Angle Dark Field (MAADF - 29-68 mrad) for γ -Al₂O₃/SrTiO₃ and in High Angle Dark Field (HAADF - 50-115 mrad) for LaAlO₃/SrTiO₃.

III. STRUCTURAL COMPARISON

HRSTEM images of LaAlO₃/SrTiO₃ (sample 5) and γ -Al₂O₃/SrTiO₃ (sample 3) are displayed in Fig. 1a) and d), respectively. These show a atomic ordering corresponding to epitaxial growth. We expect this to be representative for the entire sample consistent with the Kiessig fringes visible in XRR of Sample 4 in Supplemental Material (SM) III. As illustrated in Fig. 1b), the interface between LaAlO₃ and SrTiO₃ consists of two cubic perovskites with a lattice mismatch of 3.0%. The comparatively lower lattice constant of LaAlO₃ induces compressive strain in SrTiO₃ near the interface. Conversely, as shown in Fig. 1e), the SrTiO₃ in the interface of γ -Al₂O₃/SrTiO₃ undergoes tensile strain. This occurs since, the interface between spinel-perovskite γ -

Al₂O₃ and SrTiO₃ is composed of four SrTiO₃ unit cells (u.c.) per γ -Al₂O₃ u.c., with a lattice mismatch of only 1.3% compared to the doubled lattice parameter of STO. DFT calculated band structure of these interfaces are presented in Fig. 1c) for LaAlO₃/SrTiO₃ [3] and Fig. 1f) for γ -Al₂O₃/SrTiO₃ [4]. Here we observe an inversion of the d_{xy} and d_{xz}/yz bands in the range of the Fermi energy consistent with data from resonant soft x-ray linear dichroism[27] and angle-resolved photoemission spectroscopy.[4] In LaAlO₃/SrTiO₃, the lower band has d_{xy} -character, whereas in γ -Al₂O₃/SrTiO₃, it has d_{xz}/yz -character. This difference between d_{xy} to d_{xz}/yz as the majority band could lead to higher carrier mobilities with a weaker dependency of the oxygen vacancies generated carrier concentration in γ -Al₂O₃/SrTiO₃ compared to LaAlO₃/SrTiO₃ as described above.[4]

IV. LOW-TEMPERATURE TRANSPORT

Transport measurements of Sample 1 were performed between 20 mK and 300 K in vdP contact configuration (details in SM I) yielding the sheet resistance, R_s , as displayed in Fig. 2a). Metallic behavior, decreasing R_s with decreasing T , is observed and the high residual resistance ratio (RRR), $R_s(300\text{ K})/R_s(1.5\text{ K}) = 6915$ is consistent with high mobility at low T . [13] As the inset in Fig. 2a) shows, an upturn in sheet resistance with decreasing temperature takes place starting from 1.5 K. Similar upturns are previously described in literature as Kondo-like features, indicating electron scattering from unpaired spins.[37]

In Fig. 2b) the out-of-plane magnetoresistance, $MR = \frac{R_i(B) - R_i(0)}{R_i(0)} \times 100\%$, is shown with $i = a, b$, or s for the two vdP configurations, and the combined sheet resistance respectively. Worth noting is the resistance anisotropy between the vdP configurations,

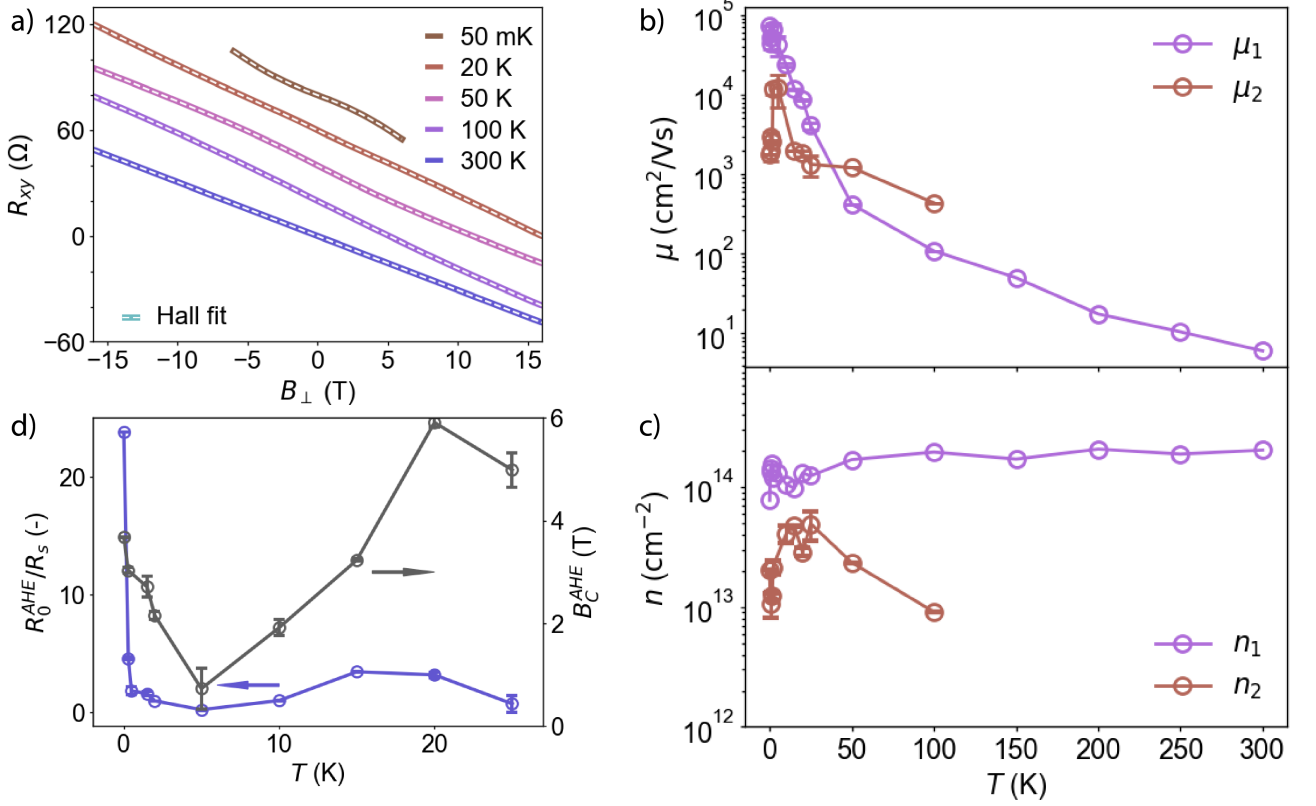


FIG. 3. Fitting of the Hall and sheet resistance data for the full temperatures 50 mK - 300 K. a) shows the data (solid coloured lines) and corresponding fits (dashed white lines), for selected temperatures ranging over the different temperature regimes described in the text. For each step down in temperature, the curves are offset by 20 Ω . The data for $T \geq 50$ K is the same as in Fig. 2c). The fitting parameters are plotted in b-d). b) is charge carrier mobilities, μ , of the two bands and, c) the corresponding densities, n_i , dependent on the temperature for sample 1. d) shows the parameters from the Anomalous Hall Effect contribution at the low-temperature regime. The lines in b-d) are guides for the eye. In b-d) points with errors exceeding a limit of the plots are hidden for clarity. The uncertainties correspond to the change in the parameter necessary to increase χ^2 with reduced χ^2 . This is chosen based on the argument that high-quality estimates of the uncertainties for this fitting procedure are unknown.[36]

$R_b(0 T)/R_a(0 T) = 0.82$ which increase with magnetic field such that $R_b(\pm 6 T)/R_a(\pm 6 T) = 2.99$. The overall magnetoresistance reaches the range of $10^3\%$ at ± 6 T in both vdP configurations and does not saturate, placing this sample in the *extreme magnetoresistance* regime.[38]. Worth noticing is the absence of features indicating weak localization (WL), which otherwise could have provided an alternative explanation to the resistance upturn below 1.5 K in Fig. 2a).[39]

Hall measurements between 300 K and 2 K, with 50 K spacing between 300 K and 50 K, are presented in Fig. 2c). Hall measurements at additional temperatures are displayed in SM II. The data shows linearity from 300 K to 150 K. At 50 and 100 K the data turns nonlinear with magnetic field-dependent slopes indicating 2-band electron transport, but at 2 K the slopes invert, consistent with AHE.[37]

Based on these observations, we separate the Hall data in the different temperature regimes, high (H), medium (M), and low (L), as follows:

$$\text{H (150 K - 300 K): } R_{xy} = R_{xy}^{1e}$$

$$\text{M (50 K - 100 K): } R_{xy} = R_{xy}^{2e}$$

$$\text{L (50 mK - 25 mK): } R_{xy} = R_{xy}^{2e} + R_{xy}^{AHE}$$

with R_{xy}^{1e} being the contribution from a single electronic band, R_{xy}^{2e} the contribution from two electronic bands, and R_{xy}^{AHE} being the contribution from AHE.

The Hall data was fitted with the contributions in the different temperature regimes. The fitting procedure, including the full equations,[37, 40] is described in SM IV. Selected fits and data across all temperatures is displayed in Fig. 3a. The fits yield carrier densities n_i , and mobilities μ_i , $i=1,2$, of the two bands (Fig. 3b,c). R_0^{AHE} and B_C^{AHE} are the AHE parameters (Fig. 3d), with R_0^{AHE} being proportional to the saturation magnetization and B_C^{AHE} being the B above which a possible magnetization perpendicular to the interface saturates. More details about the AHE contribution can

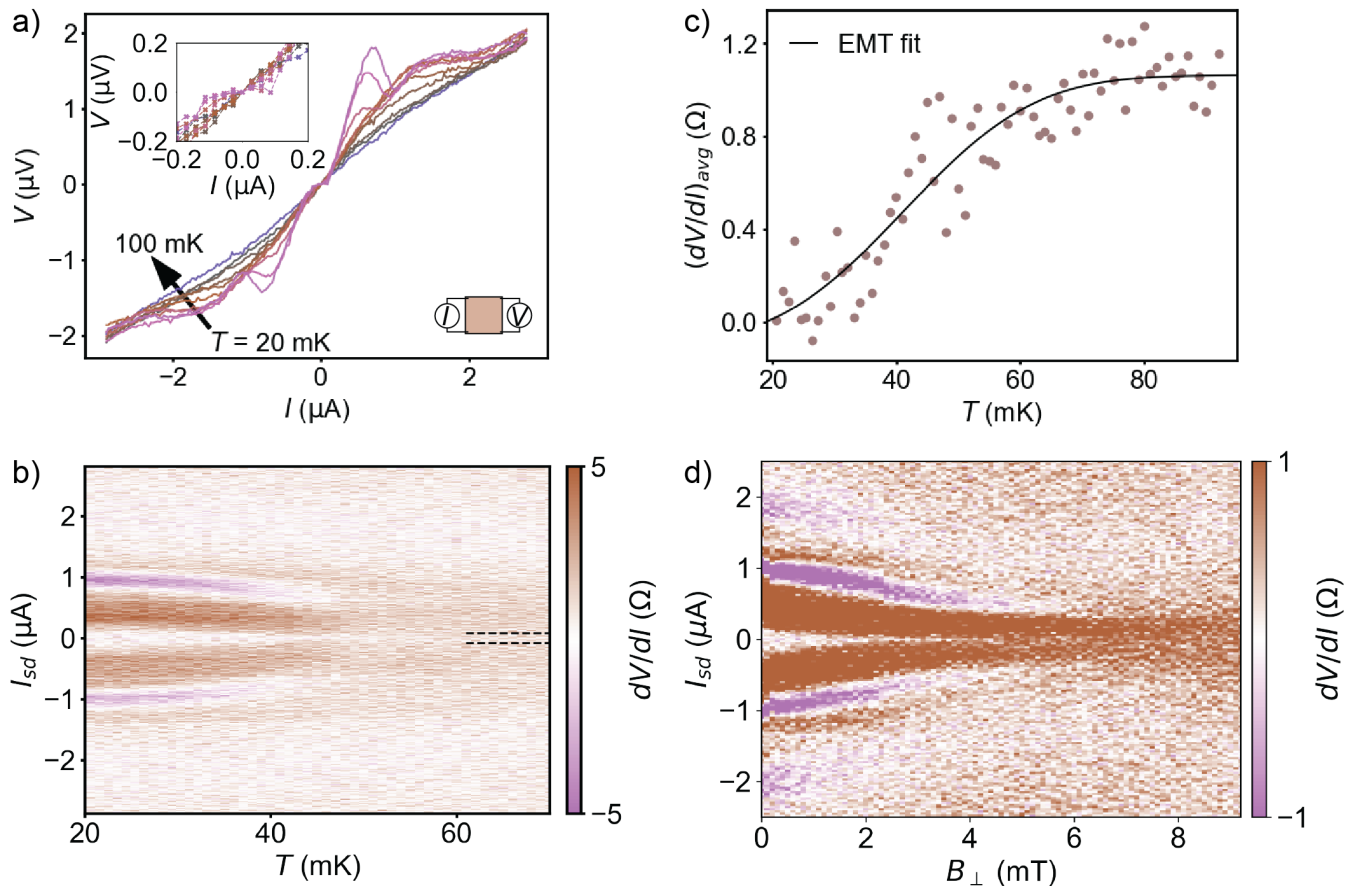


FIG. 4. Indications of superconductivity a) $V(I)$ -curves at temperatures ranging from 100 mK to 15 mK. b) Differential resistance as a function of source-drain current and temperature. c) Average dV/dI as a function of temperature, corresponding to the local resistance in b) for I_{sd} between $\pm 0.08 \mu\text{A}$, as indicated by the dashed lines in b). The line in c) is the EMT fit. The uncertainties of each fitting parameter correspond to the change in the parameter necessary to increase χ^2 with reduced χ^2_v as described in SM IV. d) Differential resistance as a function of source-drain current and out-of-plane magnetic field magnitude.

be found in ref. [37].

In Fig. 3b) μ_1 decreases with increasing temperature with a maximum of $73 \times 10^3 \text{ cm}^2/\text{Vs}$. The relation between the mobilities becomes consistent with the band-structure, i.e. $\mu_1 > \mu_2$, at $T < 50 \text{ K}$. In c) neither n_1 nor n_2 shows any temperature dependence, pointing towards the mobilities as the dominant factor of the temperature dependence of R_s . Following the connection between mobility and band structure discussed above, we attribute the high-mobility channel, n_1 and μ_1 , to the dxz/yz -band and the low-mobility channel, n_2 and μ_2 , to the dxy -band.

The densities are approximately an order of magnitude higher than comparable $\text{LaAlO}_3/\text{SrTiO}_3$ samples, where the low-density band and the high-density band are on the order of 10^{12} cm^{-2} and 10^{13} cm^{-2} respectively.[17, 41] The higher density in the $\gamma\text{-Al}_2\text{O}_3/\text{SrTiO}_3$ interface could be a result of either stabilization of oxygen vacancies in SrTiO_3 from tensile strain[42, 43] rather than the compressive strain in the SrTiO_3 of $\text{LaAlO}_3/\text{SrTiO}_3$ in SrTiO_3 , increasing the number of electron donors.

Another origin could be a stronger electric field in $\gamma\text{-Al}_2\text{O}_3$ than in LaAlO_3 causing a polar catastrophe when grown on SrTiO_3 . [44] The last origin should leave a conducting 2DEG after annealing in an oxygen-rich environment. However, annealing Sample 6 in O_2 , resulted in a transition from $R_s(300 \text{ K}) = 310 \Omega/\text{sq}$ to $R_s(300 \text{ K}) > 950 \text{ M}\Omega/\text{sq}$.

In Fig. 3d), R_0^{AHE} is normalized with R_s , but shows an increase with decreasing temperature. This is consistent with the 50 mK Hall plot displayed in Fig 3a), which has the most prominent AHE indicative slope of all the data. The B_C^{AHE} seems to be temperature independent, fluctuating below 6 T throughout the temperatures. Corresponding measurements and plots for sample 2, as displayed in SM V, showed similar results with lower magnitudes of μ and RRR , and higher n .

The observation of AHE can be explained by scattering from unpaired spins and is consistent with the Kondo-like R_s upturn below 1.5 K in Fig. 2a). The upturn could also result from freeze-out of nano- or even microscale regions of the 2DEG.[8, 9, 49–51] Since the

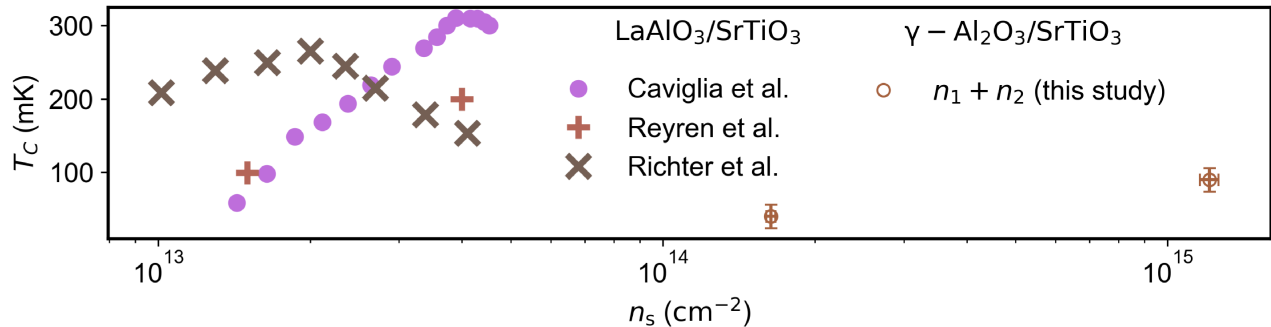


FIG. 5. Reshaping of the superconducting dome. Superconducting critical temperature, T_C , as a function of 2D carrier density for $\text{LaAlO}_3/\text{SrTiO}_3$ and $\gamma\text{-Al}_2\text{O}_3/\text{SrTiO}_3$. The $\text{LaAlO}_3/\text{SrTiO}_3$ data as adapted from refs [5, 45, 46] found in [47]. The n_s values of $\gamma\text{-Al}_2\text{O}_3/\text{SrTiO}_3$ are the average across all temperatures of the total carrier densities with an uncertainty lower than 100%. [48] This is chosen because the summed carrier densities are approximately constant with temperature. T_C values of $\gamma\text{-Al}_2\text{O}_3/\text{SrTiO}_3$ corresponds to \bar{T}_C with uncertainties being the sum of the parameter uncertainty of \bar{T}_C added, half of γ and half the parameter uncertainty of γ .

energy density of the PLD plume is highest at the centre of the plume front, where the species have travelled the least when they reach the substrate, it can be expected that the 2DEG is inhomogeneous. In addition SrTiO_3 furthermore undergoes a ferroelastic transition from cubic to tetragonal at 105 K, creating domains of different tetragonal orientations.[52] Regarding freeze-out, this is not directly consistent with the AHE signature, leaving the Kondo-like explanation as the most likely.

V. SUPERCONDUCTIVITY

At the temperatures discussed so far, the samples displayed a linear dependence of voltage, $V(I)$, on current, I . However, below $T \sim 100$ mK, nonlinearities in $V(I)$ emerge around $I = 0$ as shown in Fig. 4a). In particular, $V(I)$ remains zero for low but finite I , before rapidly increasing. This behavior is consistent with superconductivity (SC), where $R = 0$ below a critical current, I_C , temperature, T_C and magnetic field B_C . The $\sim \mu\text{A}$ scale of I_C is orders of magnitude below what would be expected for a uniform 2D superconducting sheet, and is more consistent with a Josephson Junction (JJ) I_C . Given the large sample size and lack of an intentionally defined JJ, it is likely that the sample contains a large number of superconducting puddles on the order of 200 nm, broken up by thin normal/insulating regions [8, 9, 53]. Such a morphology results in a network of random, weakly coupled JJs[42], as reported previously for both amorphous[8] and crystalline[9] $\text{LaAlO}_3/\text{SrTiO}_3$. The temperature dependence of the differential resistance, dV/dI , is shown in Fig. 4b), with the superconductivity-related non-linearities suppressed as T approaches T_C . To estimate the critical temperature,

T_C , we extract dV/dI in the range $|I| < \pm 80$ nA, as indicated by the dashed lines in Fig 4b), and display the average of this as a function of temperature in Fig. 4c). The gradual transition between the superconducting and normal state is typical for STO-based 2DEGs.

To estimate T_C , Effective Medium Theory (EMT), which has previously been shown to describe inhomogeneous superconducting oxide interfaces well [8, 49], was employed to fit the data. The method is described in ref. [49] and utilize the fitting parameters R^∞ , ω , \bar{T}_C , and γ . Here R^∞ is the high-temperature resistance, ω is the weight of the T_C distribution i.e. the fraction of SC puddles, \bar{T}_C and γ are the average and the full width at half maximum of the Gaussian distribution of puddle T_C s. From the fit we find $R^\infty = 1 \pm 0 \Omega$, $\omega = 0.6 \pm 0.1$, $\bar{T}_C = 40 \pm 5$ mK, and $\gamma = 18 \pm 5$ mK. Thus, the superconducting transitions of the puddles can be described as a Gaussian distribution with $\bar{T}_C = 40 \pm 5$ mK and $\gamma = 18 \pm 5$ mK. The value of ω is consistent with ref. [49], and the value of R^∞ is consistent with the data above the superconducting transition in Fig. 4c).

For the lowest measured $T \lesssim 40$ mK, a symmetric, but non-monotonic $V(I)$ relation is observed for $|I| > I_C$, producing regions of negative differential resistance (NDR) in dV/dI . NDR can result from Joule heating, however, this is also expected to produce hysteretic and non-symmetric $V(I)$, which we do not observe here. Rather, we suggest the NDR arises from the complex characteristics of the underlying JJ network [54].

The transition from near-zero to finite resistance with magnetic field magnitude is consistent with a critical magnetic field B_C breaking down the SC phase. This is shown as dV/dI as a function of bias current and out-of-plane magnetic field magnitude, B_\perp , in Fig. 4d). The corresponding analysis of the superconducting features of Sample 2 is displayed in SM VI.

VI. DISCUSSION

Displaying the SC critical values ($T_C/B_C/I_C$) as a function of n_S in $\text{LaAlO}_3/\text{SrTiO}_3$ typically reveal dome-like phase diagram with the onset quantum critical point (QCP) as the lowest n_S intersection with the x-axis and a maximum $T_C \check{m}ax$ as indicated in the Fig. 5).[9, 23, 45, 46]. The region between QCP and $T_C \check{m}ax$ is termed as the under-doped region and the region above $T_C \check{m}ax$ in n_S as the over-doped region.

Taking the higher average transition temperature $\bar{T}_C = 90 \pm 3$ mK of Sample 2 (S2) compared to Sample 1 (S1) into account, reveal a tendency of $T_C(n_S^{S1}) < T_C(n_S^{S2})$ for $n_S^{S1} < n_S^{S2}$. This negates that both samples are in the overdoped regime of the dome where $T_C(n_S^{S1}) > T_C(n_S^{S2})$ for $n_S^{S1} < n_S^{S2}$. While further samples are needed to outline the superconducting dome for $\gamma\text{-Al}_2\text{O}_3/\text{SrTiO}_3$ 2DEGs, we can conclude that $n_S(T_C \check{m}ax)$ of the dome is at least three times higher than that for LAO/STO, and may be orders of magnitude higher if $n_S(T_C \check{m}ax)$ exceeds that of sample 2.

Considering the band ordering of the dxy -band compared to the dxz/yz -band, we can tentatively assign the superconductivity as arising from the dxz/yz -band. If the superconductivity came from the dxy -band, the QCP would mark the onset of filling this band. Increasing n_S would increase the critical values until a maximum ($T_C \check{m}ax$) marking the start of the filling of the subsequent dxz/yz -band. This is inconsistent with the band inversion of $\gamma\text{-Al}_2\text{O}_3/\text{SrTiO}_3$, which shows superconductivity, while the dxz/yz -band is lower in energy than the dxy -band and therefore strongly dominating. Contrarily, if the superconductivity came from dxz/yz -band, the QCP would witness the onset of filling into this band and the $T_C \check{m}ax$ the filling into the dxy -band. This is consistent with the superconductivity at a broader range and even higher carrier densities than in $\text{LaAlO}_3/\text{SrTiO}_3$.

One further detail worth noting is the increasing AHE contribution at low temperatures, which keeps increasing in Sample 1 down to 50 mK below which Hall data were not measured. This temperature, however, overlaps with the Gaussian distribution describing the critical temperatures of the puddles, suggesting the co-existence of superconductivity and unpaired spins in the same temperature range in Sample 1. This is further supported by the upturn in R_S at the lowest temperatures until the superconducting transition. As previously described in ref. [41], these unpaired spins likely originate from the oxygen vacancies existing at and near the interface in $\gamma\text{-Al}_2\text{O}_3/\text{SrTiO}_3$. This is consistent with the understanding that the 2DEG is generated by electrons donated by oxygen vacancies, and they should not disappear as superconductivity arises but indeed result in an effective lowering of T_C compared to $\text{LaAlO}_3/\text{SrTiO}_3$ as indicated by Fig. 5. Additionally, because one oxygen vacancy donates one electron, the oxygen vacancy density should be on the same order of magnitude as the carrier density of

the electrons.

VII. CONCLUSION

In conclusion, this investigation has utilized the band-tunability of SrTiO_3 from the deposition of a 4 nm epitaxial $\gamma\text{-Al}_2\text{O}_3$ thin film, previously demonstrated by resonant soft X-ray linear dichroism[27] and angle-resolved photoemission spectroscopy, and calculated by DFT[4]. The perovskite thin-film provides an increase in n_S and a band inversion of the dxy - and dxz/yz -band that is located near the Fermi energy. The increase in n_S is consistent with strain stabilization of electron donating oxygen vacancies [42, 43] and the band inversion could be caused by a symmetry breaking of the Ti octahedral ordering into pyramidal ordering.[27] With this band inversion the filling of the dxz/yz -band exceeds that of the dxy -band. The mobility of the dxz/yz -band at 50 mK was found to be 7.3×10^4 cm²/Vs, higher than the typical mobilities of $\text{LaAlO}_3/\text{SrTiO}_3$. We attribute this to the higher fraction of electronic states in the dxz/yz -band dispersed further into SrTiO_3 compared to the dxy -band.

Below $T \approx 100$ mK, the $\gamma\text{-Al}_2\text{O}_3/\text{SrTiO}_3$ interfaces showed superconductivity consistent with a distribution of Josephson-Junction coupled superconducting puddles in the interface. The order-of-magnitude larger carrier density at which superconductivity was observed compared to $\text{LaAlO}_3/\text{SrTiO}_3$ suggests that the band inversion significantly reshapes the superconducting dome. Furthermore, due to the presence of superconductivity in the strongly dxz/yz -band dominated interface, it is unlikely that the dxy -band is responsible for SC transport in $\gamma\text{-Al}_2\text{O}_3/\text{SrTiO}_3$. Finally, we see indications of unpaired spins in one of the $\gamma\text{-Al}_2\text{O}_3/\text{SrTiO}_3$ samples through Anomalous Hall Effect and Kondo-like features. The Anomalous Hall Effect resistance contribution tends to increase with decreasing temperature, yielding the strongest signature at temperatures that overlaps with the Gaussian distribution of superconducting puddle T_C s. Thus the existence of superconductivity and unpaired spins, likely stemming from oxygen vacancies, in the same temperature range seems to be a property of $\gamma\text{-Al}_2\text{O}_3/\text{SrTiO}_3$.

VIII. ACKNOWLEDGEMENTS

We thank V. Rosendal, C. E. N. Petersen, R. T. Dahm, H. Witt, S. Mallik, and M. Bibes for helpful discussions. We thank Z.L. Liao and G. Koster at the University of Twente for providing the LAO/STO sample used to compare STEM images. T.H.O. and F.T. acknowledge support by research grant 37338 (SANSIT) from Villum Fonden. T.S.J. acknowledges support from the Novo Nordic Foundation Challenge Program, grant no. NNF21OC0066526 (BioMag). N.G. and J.V. ac-

knowledge funding from GOA project “Grignard 2.0” of the University of Antwerp. Z.Zhang is gratefully acknowl-

edged for image processing of the STEM image stacks.

-
- [1] A. Ohtomo and H. Y. Hwang, A high-mobility electron gas at the $\text{LaAlO}_3/\text{SrTiO}_3$ heterointerface, *Nature* **427**, 423 (2004).
- [2] Z. Rongsheng and R. Snyder, Structures and transformation mechanisms of the η , γ and θ transition aluminas, *Acta Crystallographica Section B: Structural Science* **47** (1991).
- [3] J. Zabaleta, V. S. Borisov, R. Wanke, H. O. Jeschke, S. C. Parks, B. Baum, A. Teker, T. Harada, K. Syassen, T. Kopp, N. Pavlenko, R. Valentí, and J. Mannhart, Hydrostatic pressure response of an oxide-based two-dimensional electron system, *Physical Review B* **93**, 235117 (2016).
- [4] A. Chikina, D. V. Christensen, V. Borisov, M.-A. Husanu, Y. Chen, X. Wang, T. Schmitt, M. Radovic, N. Nagao, A. S. Mishchenko, R. Valentí, N. Pryds, and V. N. Strocov, Band-order anomaly at the γ - $\text{Al}_2\text{O}_3/\text{SrTiO}_3$ interface drives the electron-mobility boost, *ACS Nano* **15**, 4347 (2021), doi: 10.1021/acsnano.0c07609.
- [5] N. Reyren, S. Thiel, A. D. Caviglia, L. F. Kourkoutis, G. Hammerl, C. Richter, C. W. Schneider, T. Kopp, A.-S. Ruetschi, D. Jaccard, M. Gabay, D. A. Müller, J.-M. Triscone, and J. Mannhart, Superconducting interfaces between insulating oxides, *Science* **317**, 1196 (2007).
- [6] G. Venditti, J. Biscaras, S. Hurand, N. Bergeal, J. Lesueur, A. Dogra, R. C. Budhani, M. Mondal, J. Jesudasan, P. Raychaudhuri, S. Caprara, and L. Benfatto, Nonlinear $i\{-\}v$ characteristics of two-dimensional superconductors: Berezinskii-kosterlitz-thouless physics versus inhomogeneity, *Physical Review B* **100**, 64506 (2019).
- [7] S. Mallik, G. C. Ménard, G. Saiz, H. Witt, J. Lesueur, A. Gloter, L. Benfatto, M. Bibes, and N. Bergeal, Superfluid stiffness of a KtO_3 -based two-dimensional electron gas, *Nature Communications* **13**, 4625 (2022).
- [8] G. E. D. K. Prawiroatmodjo, F. Trier, D. V. Christensen, Y. Chen, N. Pryds, and T. S. Jespersen, Evidence of weak superconductivity at the room-temperature grown $\text{LaAlO}_3/\text{SrTiO}_3$ interface, *Physical Review B* **93**, 184504 (2016).
- [9] S. Hurand, A. Jouan, E. Lesne, G. Singh, C. Feuillet-Palma, M. Bibes, A. Barthélémy, J. Lesueur, and N. Bergeal, Josephson-like dynamics of the superconducting $\text{LaAlO}_3/\text{SrTiO}_3$ interface, *Physical Review B* **99**, 104515 (2019).
- [10] A. Brinkman, M. Huijben, M. van Zalk, J. Huijben, U. Zeitler, J. C. Maan, W. G. van der Wiel, G. Rijnders, D. H. A. Blank, and H. Hilgenkamp, Magnetic effects at the interface between non-magnetic oxides, *Nature Materials* **6**, 493 (2007).
- [11] A. D. Caviglia, M. Gabay, S. Gariglio, N. Reyren, C. Cancellieri, and J.-M. Triscone, Tunable rashba spin-orbit interaction at oxide interfaces, *Physical Review Letters* **104**, 10.1103/physrevlett.104.126803 (2010).
- [12] Y. Z. Chen, N. Bovet, F. Trier, D. V. Christensen, F. M. Qu, N. H. Andersen, T. Kasama, W. Zhang, R. Giraud, J. Dufouleur, T. S. Jespersen, J. R. Sun, A. Smith, J. Nygård, L. Lu, B. Büchner, B. G. Shen, S. Linderöth, and N. Pryds, A high-mobility two-dimensional electron gas at the spinel/perovskite interface of γ - $\text{Al}_2\text{O}_3/\text{SrTiO}_3$, *Nature Communications* **4**, 1371 (2013).
- [13] D. V. Christensen, Y. Frenkel, P. Schutz, F. Trier, S. Wissberg, R. Claessen, B. Kalisky, A. Smith, Y. Z. Chen, and N. Pryds, Electron mobility in $\text{Al}_2\text{O}_3/\text{SrTiO}_3$, *Physical Review Applied* **9**, 10.1103/PhysRevApplied.9.054004 (2018).
- [14] D. A. Dikin, M. Mehta, C. W. Bark, C. M. Folkman, C. B. Eom, and V. Chandrasekhar, Coexistence of superconductivity and ferromagnetism in two dimensions, *Physical Review Letters* **107**, 56802 (2011).
- [15] L. Li, C. Richter, J. Mannhart, and R. C. Ashoori, Coexistence of magnetic order and two-dimensional superconductivity at $\text{LaAlO}_3/\text{SrTiO}_3$ interfaces, *Nature Physics* **7**, 762 (2011).
- [16] J. A. Bert, B. Kalisky, C. Bell, M. Kim, Y. Hikita, H. Y. Hwang, and K. A. Moler, Direct imaging of the coexistence of ferromagnetism and superconductivity at the $\text{LaAlO}_3/\text{SrTiO}_3$ interface, *Nature Physics* **7**, 767 (2011).
- [17] F. Trier, D. C. Vaz, P. Bruneel, P. Noël, A. Fert, L. Vila, J.-P. Attané, A. Barthélémy, M. Gabay, H. Jaffrès, and M. Bibes, Electric-field control of spin current generation and detection in ferromagnet-free SrTiO_3 -based nanodevices, *Nano Letters* **20**, 395 (2020), doi: 10.1021/acsnanolett.9b04079.
- [18] P. Noël, F. Trier, L. M. V. Arce, J. Bréhin, D. C. Vaz, V. Garcia, S. Fusil, A. Barthélémy, L. Vila, M. Bibes, and J.-P. Attané, Non-volatile electric control of spin-charge conversion in a SrTiO_3 rashba system, *Nature* **580**, 483 (2020).
- [19] D. C. Vaz, F. Trier, A. Dyrdał, A. Johansson, K. Garcia, A. Barthélémy, I. Mertig, J. Barnaś, A. Fert, and M. Bibes, Determining the rashba parameter from the bilinear magnetoresistance response in a two-dimensional electron gas, *Physical Review Materials* **4**, 71001 (2020).
- [20] A. Jouan, G. Singh, E. Lesne, D. C. Vaz, M. Bibes, A. Barthélémy, C. Ulysse, D. Stornaiuolo, M. Salluzzo, S. Hurand, J. Lesueur, C. Feuillet-Palma, and N. Bergeal, Quantized conductance in a one-dimensional ballistic oxide nanodevice, *Nature Electronics* **3**, 201 (2020).
- [21] G. Singh, G. Venditti, G. Saiz, G. Herranz, F. Sánchez, A. Jouan, C. Feuillet-Palma, J. Lesueur, M. Grilli, S. Caprara, and N. Bergeal, Two-gap $\{s\}\pm\{d\}$ -wave superconductivity at an oxide interface, *Physical Review B* **105**, 64512 (2022).
- [22] G. Singh, A. Jouan, G. Herranz, M. Scigaj, F. Sánchez, L. Benfatto, S. Caprara, M. Grilli, G. Saiz, F. Couëdo, C. Feuillet-Palma, J. Lesueur, and N. Bergeal, Gap suppression at a lifshitz transition in a multi-condensate superconductor, *Nature Materials* **18**, 948 (2019).
- [23] A. Jouan, S. Hurand, G. Singh, E. Lesne, A. Barthélémy, M. Bibes, C. Ulysse, G. Saiz, C. Feuillet-Palma, J. Lesueur, and N. Bergeal, Multiband effects in the superconducting phase diagram of oxide inter-

- faces, *Advanced Materials Interfaces* **9**, 2201392 (2022), <https://doi.org/10.1002/admi.202201392>.
- [24] G. Singh, C. Guarcello, E. Lesne, D. Winkler, T. Claesson, T. Bauch, F. Lombardi, A. D. Caviglia, R. Citro, M. Cuoco, and A. Kalaboukhov, Gate-tunable pairing channels in superconducting non-centrosymmetric oxides nanowires, *npj Quantum Materials* **7**, 2 (2022).
- [25] M. Salluzzo, J. C. Cezar, N. B. Brookes, V. Bisogni, G. M. D. Luca, C. Richter, S. Thiel, J. Mannhart, M. Huijben, A. Brinkman, G. Rijnders, and G. Ghiringhelli, Orbital reconstruction and the two-dimensional electron gas at the $\text{LaAlO}_3/\text{SrTiO}_3$ interface, *Physical Review Letters* **102**, 166804 (2009).
- [26] P. Delugas, A. Filippetti, V. Fiorentini, D. I. Bilc, D. Fontaine, and P. Ghosez, Spontaneous 2-dimensional carrier confinement at the n -type $\text{LaAlO}_3/\text{SrTiO}_3$ interface, *Physical Review Letters* **106**, 166807 (2011).
- [27] Y. Cao, X. Liu, P. Shafer, S. Middey, D. Meyers, M. Kareev, Z. Zhong, J.-W. Kim, P. J. Ryan, E. Arenholz, and J. Chakhalian, Anomalous orbital structure in a spinel-perovskite interface, *npj Quantum Materials* **1**, 16009 (2016).
- [28] J. R. L. Mardegan, D. V. Christensen, Y. Z. Chen, S. Parchenko, S. R. V. Avula, N. Ortiz-Hernandez, M. Decker, C. Piamonteze, N. Pryds, and U. Staub, Magnetic and electronic properties at the $\gamma\text{-Al}_2\text{O}_3/\text{SrTiO}_3$ interface, *Physical Review B* **99**, 134423 (2019).
- [29] W. Niu, Y.-W. Fang, R. Liu, Z. Wu, Y. Chen, Y. Gan, X. Zhang, C. Zhu, L. Wang, Y. Xu, Y. Pu, Y. Chen, and X. Wang, Fully optical modulation of the two-dimensional electron gas at the $\gamma\text{-Al}_2\text{O}_3/\text{SrTiO}_3$ interface, *The Journal of Physical Chemistry Letters* **13**, 2976 (2022), doi: 10.1021/acs.jpcclett.2c00384.
- [30] S. Su, J. H. You, and C. Lee, Electron transport at interface of LaAlO_3 and SrTiO_3 band insulators, *Journal of Applied Physics* **113**, 093709 (2013).
- [31] A. F. Zurhelle, D. V. Christensen, S. Menzel, and F. Gunkel, Dynamics of the spatial separation of electrons and mobile oxygen vacancies in oxide heterostructures, *Physical Review Materials* **4**, 104604 (2020).
- [32] Y. Z. Chen, F. Trier, T. Wijnands, R. J. Green, N. Gauquelin, R. Egoavil, D. V. Christensen, G. Koster, M. Huijben, N. Bovet, S. Macke, F. He, R. Sutarto, N. H. Andersen, J. A. Sulpizio, M. Honig, G. E. D. K. Prawiroatmodjo, T. S. Jespersen, S. Linderoth, S. Ilani, J. Verbeeck, G. Van Tendeloo, G. Rijnders, G. A. Sawatzky, and N. Pryds, Extreme mobility enhancement of two-dimensional electron gases at oxide interfaces by charge-transfer-induced modulation doping, *Nature Materials* **14**, 801 (2015).
- [33] M. Huijben, G. Koster, M. K. Kruize, S. Wenderich, J. Verbeeck, S. Bals, E. Slooten, B. Shi, H. J. A. Molegraaf, J. E. Kleibeuker, S. van Aert, J. B. Goedkoop, A. Brinkman, D. H. A. Blank, M. S. Golden, G. van Tendeloo, H. Hilgenkamp, and G. Rijnders, Defect engineering in oxide heterostructures by enhanced oxygen surface exchange, *Advanced Functional Materials* **23**, 5240 (2013), <https://doi.org/10.1002/adfm.201203355>.
- [34] A. J. H. van der Torren, Z. Liao, C. Xu, N. Gauquelin, C. Yin, J. Aarts, and S. J. van der Molen, Formation of a conducting $\text{LaAlO}_3/\text{SrTiO}_3$ interface studied by low-energy electron reflection during growth, *Physical Review Materials* **1**, 75001 (2017).
- [35] L. S. CO., Strontium titanate.
- [36] M. Newville, T. Stensitzki, D. B. Allen, and A. Ingargiola, *LMFIT: Non-Linear Least-Square Minimization and Curve-Fitting for Python* (2015).
- [37] F. Gunkel, C. Bell, H. Inoue, B. Kim, A. G. Swartz, T. A. Merz, Y. Hikita, S. Harashima, H. K. Sato, M. Minohara, S. Hoffmann-Eifert, R. Dittmann, and H. Y. Hwang, Defect control of conventional and anomalous electron transport at complex oxide interfaces, *Physical Review X* **6**, 31035 (2016).
- [38] D. V. Christensen, T. S. Steegemans, T. D. Pomar, Y. Z. Chen, A. Smith, V. N. Strocov, B. Kalisky, and N. Pryds, Extreme magnetoresistance at high-mobility oxide heterointerfaces with dynamic defect tunability, *Nature Communications* **15**, 4249 (2024).
- [39] W. Niu, M. Gao, X. Wang, F. Song, J. Du, X. Wang, Y. Xu, and R. Zhang, Evidence of weak localization in quantum interference effects observed in epitaxial $\text{La}_{0.7}\text{Sr}_{0.3}\text{MnO}_3$ ultrathin films, *Scientific Reports* **6**, 26081 (2016).
- [40] M. J. Kane, N. Apsley, D. A. Anderson, L. L. Taylor, and T. Kerr, Parallel conduction in $\text{GaAs}/\text{Al}_x\text{Ga}_{1-x}\text{As}$ modulation doped heterojunctions, *Journal of Physics C: Solid State Physics* **18**, 5629 (1985).
- [41] D.-S. Park, A. D. Rata, I. V. Maznichenko, S. Ostanin, Y. L. Gan, S. Agrestini, G. J. Rees, M. Walker, J. Li, J. Herrero-Martin, G. Singh, Z. Luo, A. Bhatnagar, Y. Z. Chen, V. Tileli, P. Muralt, A. Kalaboukhov, I. Mertig, K. Dörr, A. Ernst, and N. Pryds, The emergence of magnetic ordering at complex oxide interfaces tuned by defects, *Nature Communications* **11**, 3650 (2020).
- [42] U. Aschauer, R. Pfenninger, S. M. Selbach, T. Grande, and N. A. Spaldin, Strain-controlled oxygen vacancy formation and ordering in CaMnO_3 , *Physical Review B* **88**, 54111 (2013).
- [43] Z. Lan, T. Vegge, and I. E. Castelli, Exploring the electronic properties and oxygen vacancy formation in SrTiO_3 under strain, *Computational Materials Science* **231**, 112623 (2024).
- [44] D. V. Christensen and A. Smith, Is Al_2O_3 polar?, *Applied Surface Science* **423**, 887 (2017).
- [45] C. Richter, H. Boschker, W. Dietsche, E. Fillis-Tsirakis, R. Jany, F. Loder, L. F. Kourkoutis, D. A. Muller, J. R. Kirtley, C. W. Schneider, and J. Mannhart, Interface superconductor with gap behaviour like a high-temperature superconductor, *Nature* **502**, 528 (2013).
- [46] A. D. Caviglia, S. Gariglio, N. Reyren, D. Jaccard, T. Schneider, M. Gabay, S. Thiel, G. Hammerl, J. Mannhart, and J.-M. Triscone, Electric field control of the $\text{LaAlO}_3/\text{SrTiO}_3$ interface ground state, *Nature* **456**, 624 (2008).
- [47] S. N. Klimin, J. Tempere, J. T. Devreese, and D. van der Marel, Interface superconductivity in $\text{LaAlO}_3/\text{SrTiO}_3$ heterostructures, *Physical Review B* **89**, 184514 (2014).
- [48] E. O. LEBIGOT, Uncertainties: a python package for calculations with uncertainties.
- [49] S. Caprara, J. Biscaras, N. Bergeal, D. Bucheli, S. Hurand, C. Feuillet-Palma, A. Rastogi, R. C. Budhani, J. Lesueur, and M. Grilli, Multiband superconductivity and nanoscale inhomogeneity at oxide interfaces, *Physical Review B* **88**, 20504 (2013).
- [50] B. Kalisky, E. M. Spanton, H. Noad, J. R. Kirtley, K. C. Nowack, C. Bell, H. K. Sato, M. Hosoda, Y. Xie, Y. Hikita, C. Woltmann, G. Pfanzelt, R. Jany, C. Richter, H. Y. Hwang, J. Mannhart, and K. A. Moler,

- Locally enhanced conductivity due to the tetragonal domain structure in $\text{LaAlO}_3/\text{SrTiO}_3$ heterointerfaces, *Nature Materials* **12**, 1091 (2013).
- [51] M. Honig, J. A. Sulpizio, J. Drori, A. Joshua, E. Zeldov, and S. Ilani, Local electrostatic imaging of striped domain order in $\text{LaAlO}_3/\text{SrTiO}_3$, *Nature Materials* **12**, 1112 (2013).
- [52] Y. Frenkel, N. Haham, Y. Shperber, C. Bell, Y. Xie, Z. Chen, Y. Hikita, H. Y. Hwang, E. K. H. Salje, and B. Kalisky, Imaging and tuning polarity at SrTiO_3 domain walls, *Nature Materials* **16**, 1203 (2017).
- [53] J. Biscaras, N. Bergeal, S. Hurand, C. Feuillet-Palma, A. Rastogi, R. C. Budhani, M. Grilli, S. Caprara, and J. Lesueur, Multiple quantum criticality in a two-dimensional superconductor, *Nature Materials* **12**, 542 (2013).
- [54] N. F. Pedersen and S. Madsen, Thz generation using fluxon dynamics in high temperature superconductors, *IEEE Transactions on Applied Superconductivity* **19**, 726 (2009).